Hindawi
Journal of Sensors
Volume 2024, Article ID 9761684, 1 page
https://doi.org/10.1155/2024/9761684

Retraction

Retracted: Correlation Analysis between El Niño and Regional Water Vapor Characteristics Based on Intelligent Sensor and Walktrap Algorithm

Journal of Sensors

Received 23 January 2024; Accepted 23 January 2024; Published 24 January 2024

This article has been retracted by Hindawi following an investigation undertaken by the publisher [1]. This investigation has uncovered evidence of one or more of the following indicators of systematic manipulation of the publication process:

(1) Discrepancies in scope
(2) Discrepancies in the description of the research reported
(3) Discrepancies between the availability of data and the research described
(4) Inappropriate citations
(5) Incoherent, meaningless and/or irrelevant content included in the article
(6) Manipulated or compromised peer review

The presence of these indicators undermines our confidence in the integrity of the article's content and we cannot, therefore, vouch for its reliability. Please note that this notice is intended solely to alert readers that the content of this article is unreliable. We have not investigated whether authors were aware of or involved in the systematic manipulation of the publication process.

Wiley and Hindawi regrets that the usual quality checks did not identify these issues before publication and have since put additional measures in place to safeguard research integrity.

We wish to credit our own Research Integrity and Research Publishing teams and anonymous and named external researchers and research integrity experts for contributing to this investigation.

The corresponding author, as the representative of all authors, has been given the opportunity to register their agreement or disagreement to this retraction. We have kept a record of any response received.

References

[1] T. Huo and M. Li, "Correlation Analysis between El Niño and Regional Water Vapor Characteristics Based on Intelligent Sensor and Walktrap Algorithm," *Journal of Sensors*, vol. 2022, Article ID 2769123, 11 pages, 2022.

Hindawi
Journal of Sensors
Volume 2022, Article ID 2769123, 11 pages
https://doi.org/10.1155/2022/2769123

Research Article

Correlation Analysis between El Niño and Regional Water Vapor Characteristics Based on Intelligent Sensor and Walktrap Algorithm

Tingyu Huo[1] **and Mingkui Li**[2]

[1]*The College of Oceanic and Atmospheric Sciences, Ocean University of China, Qingdao, Shandong 266100, China*
[2]*Key Laboratory of Physical Oceanography, Ministry of Education, Ocean University of China, Qingdao, Shandong 266100, China*

Correspondence should be addressed to Tingyu Huo; huotingyu@stu.ouc.edu.cn

Received 25 July 2022; Revised 15 August 2022; Accepted 18 August 2022; Published 8 September 2022

Academic Editor: Gengxin Sun

Water vapor is an important part of the atmospheric system and plays a key role in the global water cycle, energy balance, extreme weather, and long-term climate research. It is of great significance to fully grasp the spatial and temporal distribution characteristics of water vapor for the study of various climate models. The traditional water vapor detection technology mainly has the problems of low spatial-temporal resolution and poor capture of fine changes. In recent decades, the rapid development of intelligent sensor technology and Walktrap algorithm has made it a reliable means to obtain and analyze the characteristics of water vapor. However, the acquisition of atmospheric water vapor requires two key parameters: station pressure (PS) and weighted average temperature (TM). Since most traditional stations are mainly used for geodetic research, few are equipped with meteorological intelligent sensors. Therefore, based on the traditional meteorological stations, this paper improves the equipment of the traditional stations and endows the traditional stations with precise and sensitive intelligent sensor equipment to obtain the regional water vapor characteristic data of El Niño and a province in the east of China, combined with the advanced Walktrap algorithm, in order to use the above equipment and technology to realize the correlation analysis of El Niño and regional water vapor characteristics. The results show that through the water vapor information calculated by 12 coastal stations, the relationship between monthly average PWV and seawater surface temperature is studied, and the correlation degree between the relevant characteristics is as high as 94.6%.

1. Introduction

Atmospheric water vapor, also known as atmospheric precipitable water, is a very important active component of the atmospheric system although its content in the atmosphere is very small [1–3]. The water vapor in the atmosphere is complex and changeable, and there are many states such as rain, snow, fog, cloud, dew, and frost. Its content fluctuates in a large range (0-4%), which is an important factor affecting the weather. The change of water vapor content is closely related to the formation of natural disasters, El Niño, rainstorm, and other extreme weather [4–6]. On the one hand, the thermal change caused by the phase change of water vapor can change the movement of the atmosphere and affect the stability of the atmosphere; on the other hand, water vapor is directly related to precipitation, affecting surface evaporation and atmospheric circulation [7]. Relevant research shows that the role of water vapor in the atmosphere is very obvious. It is a gas that can directly reflect the greenhouse effect. Once there is too much water vapor, it will accelerate global warming and cause glacier melting [8–10]. Monitoring water vapor content and activity status is of great significance for weather prediction and global climate prediction [11, 12]. Since the water vapor in the troposphere accounts for about 99% of the total atmospheric water vapor, accurate acquisition of water vapor information

over the troposphere has a significant effect on rainstorm monitoring and extreme weather warning [13].

Pacific ENSO is a strong interaction phenomenon between the tropical Pacific Ocean and the atmosphere on the interannual time scale. It is defined as the large-scale continuous warming of the surface SST in the equatorial Middle East Pacific, which has a significant impact on the distribution of atmospheric water vapor on the global scale [14]. It has been one of the hot issues studied by scholars for a long time. The El Niño morphology has changed significantly since the 1990s. In typical eastern-type El Niño events, that is, the tropical Pacific warming region is mainly located in the tropical eastern Pacific region, and the probability of El Niño events is getting smaller and smaller, while another kind of warming region is mainly located in the equatorial central Pacific near the sun line, but the warming phenomenon is occurring more and more frequently [15]. Many scholars have noticed the change of El Niño, a warming area, and call the El Niño event located in the equatorial central Pacific region as the central El Niño event [16], or the El Niño event at the solar boundary [17], or E1 Niño Modoki [15], or the warm pool El Niño event [18].

Because there are obvious differences in the sea surface temperature warming areas of the two types of El Niño events, the warming areas of the tropical ocean to the atmosphere have also changed, and the tropical atmospheric circulation conditions will be significantly different, resulting in different climatic effects. This phenomenon has also attracted extensive attention of scientists. Since Weng et al. [17] pointed out that the frequency of central El Niño events increased significantly after the 1990s, there are more and more international studies on the impact of different distribution types of El Niño events on climate anomalies. For example, some scientists have concluded that the impact of the central El Niño event on the climate of the west coast of North America, South America, and even Japan and New Zealand may be completely opposite to the impact of the eastern El Niño event [19–21]. The central-type El Niño event will also lead to the "seesaw" climate distribution characteristics of dry in the north and wet in the south in winter in the western United States. When the eastern-type El Niño occurs, most parts of the western United States are mainly wet in winter [22]. There are also many studies on the climate anomalies in East Asia, especially in China, caused by different types of El Niño events. For example, the two types of El Niño events can have different effects on the autumn precipitation in China in the development year [23–25] and the spring and summer precipitation in China in the next year [26–28] through the different interactions between the sea and air in the tropical western Pacific.

In view of the important value of atmospheric water vapor, meteorologists began to try various methods to obtain water vapor to study its spatial-temporal distribution. Traditional methods of detecting atmospheric water vapor mainly include radio sounding, meteorological satellite detection, water vapor radiometer, and solar spectrum analyzer [29]. Due to its low spatial-temporal resolution, this traditional technology has certain limitations in acquiring fine changes. With the rapid growth of modern meteorological application demand, the shortcomings of these traditional technologies are becoming more and more obvious. In order to overcome the shortcomings of these technologies, this paper analyzes the correlation between El Niño and atmospheric water vapor characteristics through intelligent sensor technology and Walktrap algorithm, in order to grasp the impact of two types of El Niño events on the relationship with autumn precipitation in southern China.

2. Two Kinds of El Niño Events and Related Basic Theories

2.1. Introduction to El Niño. El Niño Southern Oscillation (ENSO) is a complex ocean atmosphere interaction event in the low-latitude tropical Pacific region. Due to the mutual restriction between the ocean and the atmosphere, ENSO shows certain periodic cycle characteristics. El Niño is the warm phase of ENSO cycle, and La Nina is the cold phase of the ENSO cycle. At the same time, ENSO is also a natural phenomenon that breaks the normal weather pattern, resulting in severe drought, floods, tropical cyclones, forest fires, and other extreme weather. During the occurrence of El Niño, the sea-level temperature in the eastern tropical Pacific was abnormally higher than the average temperature, and the evaporation rate was fast, which brought heavy precipitation events to Latin America. During the La Nina phenomenon, heavy rainfall and storm events occurred in the western tropical Pacific. Larkin and Harrison [18] found that global warming will increase the frequency of ENSO and cause extreme weather. Studying the difference of atmospheric water vapor and combining the correlation of other ocean variables will help to explore the mechanism of ENSO evolution and reduce the social and economic losses caused by extreme disaster weather.

2.2. Division of Two Types of El Niño Events. At present, there are many studies and methods on the division of two types of El Niño events in the world. This paper uses the eastern and central indexes of ward [30] to distinguish two types of El Niño events. The index is defined as

$$\begin{cases} \mathrm{IEP} = N_3 - \alpha N_4, \\ \mathrm{ICP} = N_4 - \alpha N_3, \end{cases} \tag{1}$$

where

$$\alpha = \begin{cases} \dfrac{2}{5} & N_3 N_4 > 0, \\ 0 & N_3 N_4 \leqslant 0. \end{cases} \tag{2}$$

N_3 and N_4, respectively, represent the average sea surface temperature anomaly in nino3 area (5° S~5° N, 150° W~90° W) and nino4 area (5° S~5° N, 160° E~150° W), which are nonlinear variation parameters. In this way, we can get the monthly IEP and ICP indexes from January 1951 to December 2015. This paper discusses the impact of two types of El Niño events on autumn precipitation in the south, and the SST in the same period is also considered.

The IEP and ICP indexes in autumn are the average IEP and ICP indexes from September to November every year.

2.3. Intelligent Sensor Technology

2.3.1. Concept of Intelligent Sensor. The concept of intelligent sensor is an intelligent device that integrates sensors, actuators, and electronic circuits [32–34] or a device that integrates sensing elements and microprocessors and has monitoring and processing functions. The main feature of intelligent sensor is to output digital signals for subsequent calculation and processing. The functions of intelligent sensor include signal sensing, signal processing, data verification and interpretation, and signal transmission and conversion. The main components include a/D and D/A converters, transceivers, microcontrollers, and amplifiers.

At present, the sensor has gone through three stages of development: before 1969, it belonged to the first stage, mainly manifested as structural sensors. The 20 years after 1969 belong to the second stage, mainly represented by solid-state sensors. From 1990 to now, it belongs to the third stage, mainly represented by intelligent sensors.

The composition diagram of intelligent sensor is shown in Figure 1. The data conversion is completed in the sensor module. In this way, the two-way connections between microcontrollers are digital signals, and programmable read-only memory (PROM) can be used for digital compensation. The main features of intelligent sensors are two-way communication of instructions and data, all digital transmission, local digital processing, self-test, user-defined algorithm, and compensation algorithm.

2.3.2. Characteristics of Intelligent Sensor. Intelligent sensors are characterized by high precision, high resolution, high reliability, high adaptability, and high cost performance. Intelligent sensor obtains high signal-to-noise ratio through digital processing to ensure high accuracy. Through data fusion [32] and neural network technology, it can ensure the measurement and resolution ability of specific parameters in the multiparameter state. Through automatic compensation, the system characteristic drift caused by working conditions and environmental changes is eliminated, and the transmission speed is optimized to make the system work in the optimal low-power state, so as to improve its reliability. Through mathematical processing by software, the intelligent sensor has the functions of judgment, analysis, and processing, and the system has high adaptability. Integrated circuit technology and MEMS technology that can be produced in large scale can be adopted, with high cost performance.

2.4. Walktrap Algorithm. Walktrap community detection method relies on random walk to divide the network into communities. There is no accepted definition of community so far. In fact, the specific definition of community first depends on the specific system or the scenario we want to apply. Subjectively, there must be more connections between nodes in the community, but less connections with the rest of the network. This is also the most recognized definition of most community issues. However, from another perspective, the formation process of the community is usually defined by the algorithm. In the absence of prior information, the community is the final product of the implementation of the detection algorithm. It was proposed by [30] and has been implemented in the igraph library, which can be applied to weighted networks. Its basic network structure is shown in Figure 2.

At each step, the transition probability is from nodes$i$to$j$ is, where$P_{ij} = Y_{ij}^{k}/d(i)$;$d(i)$is the degree of node$i$. Therefore, the transition matrix of random walk is defined as $P = (P_{ij}) = D^{-1}Y^{k}$, where D is the diagonal matrix $(D_{ii} = d(i), D_{ij} = 0$, if $i \neq j)$ of degree. In a random walk of length t, the probability from nodes i to y is $(P^{t})_{ij}$, which is recorded as ${P_{ij}}^{t}$. Generally speaking, in step t of random walk, the probability of community C reaching node $j \notin C$ can be written as

$$P_{Cj}^{t} = \frac{1}{|C|}\sum_{i \in C} P_{ij}^{t}, \tag{3}$$

where $|C|$ is the sum of the number of nodes in community C.

We can get the distance between node i and node j and the distance between communities C1 and C2:

$$\begin{aligned} r_{ij}^{2} &= \sum_{k=1}^{n} \frac{\left(P_{ik}^{t} - P_{jk}^{t}\right)^{2}}{d(k)}, \\ r_{\mathrm{C1C2}}^{2} &= \sum_{k=1}^{n} \frac{\left(P_{\mathrm{C1}k}^{t} - P_{\mathrm{C2}k}^{t}\right)^{2}}{d(k)}. \end{aligned} \tag{4}$$

After calculating the distance between all pairs of communities, the Walktrap algorithm adopts the aggregation method based on Ward method [31]. Initially, a single node represents a community, that is, partition: $\mathscr{P}_1 = \{\{v\}, v \in V\}$. Then, repeat the following operation for the partition. In each step m, if the new partition minimizes the average value σ_k of the square distance between each node and its community, we will merge the two communities C1 and C2 to get a new partition. σ_k is the distance from each node to its community:

$$\sigma_k = \frac{1}{n}\sum_{C}\sum_{i \in C} r_{iC}^{2}. \tag{5}$$

These two communities merge into a new communityC3 = C1 ∪ C2and get a new partition:$\mathscr{P}_{m+1} = (\mathscr{P}_m \setminus \{\mathrm{C1}, \mathrm{C2}\}) \cup \{\mathrm{C3}\}$. Then, repeat the process until all points are merged into a community. Each step defines a partition $\mathscr{P}_m$ of the network as a community, which gives a hierarchical structure of the community called a tree view. Finally, select the optimal partition according to the maximum modularity:

$$Q(\mathscr{P}) = \sum_{C \in \mathscr{P}} e_C - a_C^{2}, \tag{6}$$

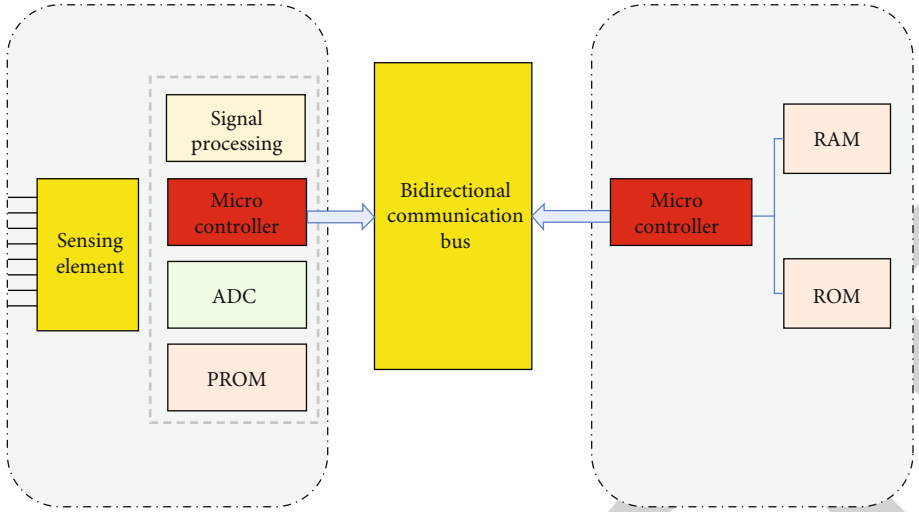

Figure 1: Composition diagram of intelligent sensor.

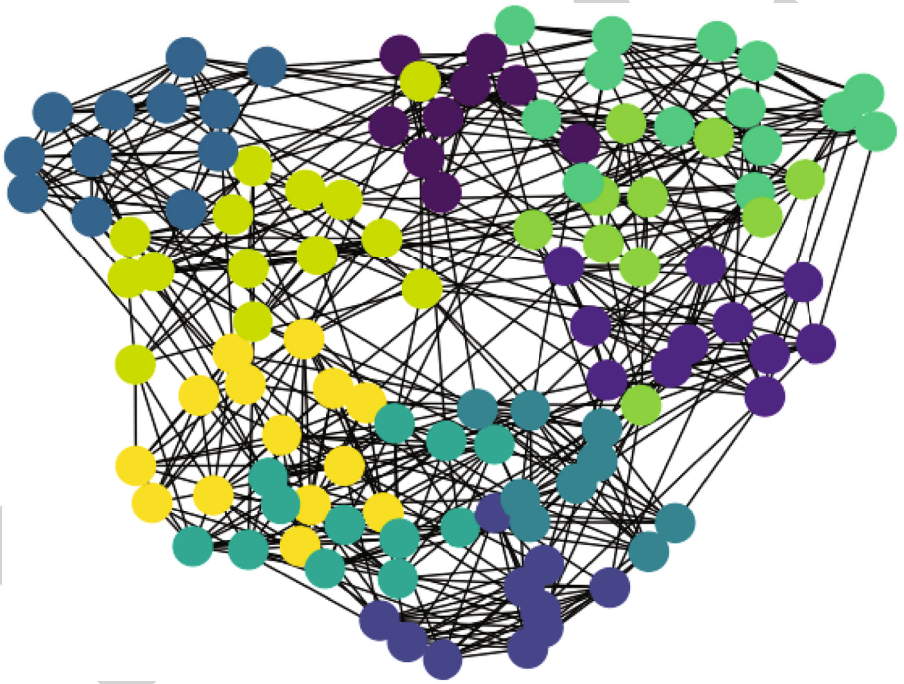

Figure 2: Walktrap algorithm basic structure chart.

where e_C is the proportion of edges in community C and a_C is the proportion of edges connected with community C.

3. Introduction to Regional Water Vapor Characteristics of Intelligent Sensor Platform

The overall design of the information acquisition platform includes five parts: sensor array hardware circuit design, sensor air chamber and air circuit design, custom TEDS design, acquisition system software design, and custom communication protocol. As shown in Figure 3 of the frame, the water is filtered after the intake pipe enters the air and injected into the air chamber of the sensor array through the air pump. The gas chamber is formed by a circuit board containing a gas sensor and an upper cover.

3.1. Single-Chip Microcomputer Selection. Internationally, the combination of a single-chip microcomputer and an off-chip ROM is often used to design stim; that is, the designed TEDS table is stored in the extended memory and operated by a microprocessor. With system on chip (with the advancement of SOC concept and the improvement of the cost performance of the single-chip microcomputer, the TEDS table can be stored in the on-chip storage

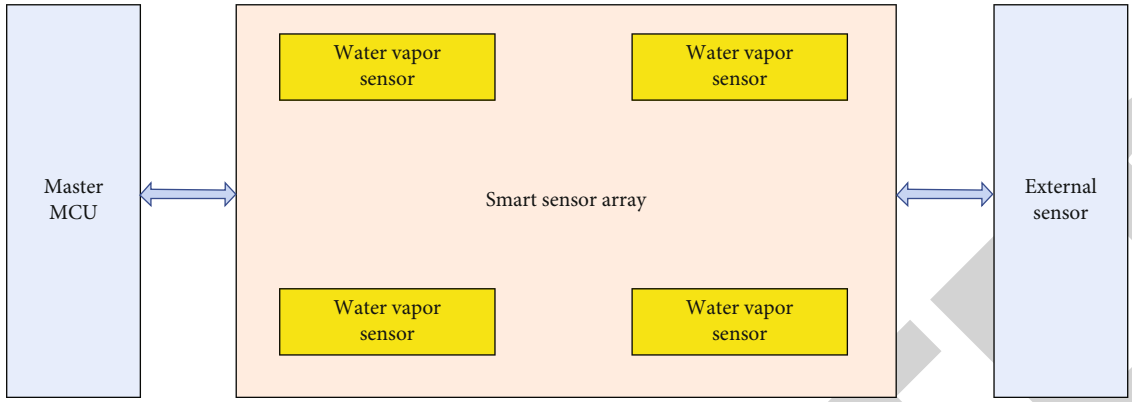

Figure 3: System data acquisition framework.

Table 1: PE port function description.

Port pin	Pin function
PE0	RXD0/PD1
PE1	TXD0/PD0
PE2	XCK0/AIN0
PE3	0C3A/AIN1
PE4	0C3B/INT4
PE5	0C3C/INT5
PE6	T3/INT
PE7	T/C3

space. This design selects an ATmega128 single-chip microcomputer, which is an 8-bit microprocessor with high performance and low power consumption. It achieves the highest performance when working at 16 mhz, so 16 mhz external crystal oscillator is used in circuit design. Its nonvolatile program and data memory has become an ideal space for TEDS data storage, including 128 K flash memory and 4 K word EEPROM segment. The processor has two programmable USARTs to realize the serial communication function. The PE pins and functions are shown in Table 1 below, in which the second multiplexing function of the port is not described in detail.

The single-chip microcomputer has 8 channels of 10-bit ADC, and the function is realized by a PF port, as shown in Figure 4. The ADC conversion module inside the single-chip microcomputer is connected with the pin to realize the input of data voltage signal. As shown in the figure, AVCC, AGND, and AREF provide working voltage, working ground, and reference voltage for the converter, respectively.

3.2. Selection of Water Vapor Sensor. The hollow fiber was first proposed by Worrell et al. [34]. The hollow fiber is coated with high-reflectivity materials, and the incident light propagates inside the fiber by reflecting back and forth inside the fiber. As early as 1992, Worrell et al. [35] measured the absorption of ethylene gas by using a 0.5 m long hollow fiber as a gas pool. The experimental results can detect ethylene gas in the order of ppmv. Compared with other sensors, such as fiber Bragg grating sensors, under the same effective optical path, because the volume of hollow fiber is much smaller than the traditional gas cell and it is relatively soft, with low optical transmission loss, small volume, easy to bend, and other characteristics, it is an ideal gas cell in the absorption spectrum measurement system. In wavelength modulation technology, because the second harmonic signal is more obvious under low voltage, the detection sensitivity of the system is also lower. Therefore, in this paper, the sensor is mainly used for the real-time measurement of water vapor in the actual atmospheric field.

The schematic diagram of the water vapor measurement device of the hollow fiber sensor is shown in Figure 5. The dew point generator is added to the path part for the gas concentration calibration during the atmospheric water vapor measurement. In the figure, the water vapor filter is connected with a stop valve, which is turned off during the water vapor calibration and turned on when measuring the actual atmospheric water vapor. The difference in the optical path part is that the air tank is replaced by the hollow fiber sensor from the one-way tank.

4. Correlation Analysis between El Niño and Regional Water Vapor Characteristics

4.1. Data Sources. The data used in this paper include the horizontal wind speed vector field (U, V) and vertical velocity field of 12 levels of monthly average provided by NCEP/NCAR (ω) And specific humidity field data, with a spatial resolution of $2.5^\circ \times 2.5^\circ$ longitude and latitude grid [32, 33]. SST field data are from SST extended reconstruction data of NOAA Climate Diagnosis Center, with a horizontal grid spacing of $2.0^\circ \times 2.0^\circ$ longitude and latitude grid. In addition, the monthly average precipitation data of 12 stations in China provided by the National Climate Center were also used. The above data period is from January 1951 to December 2018. Autumn in this paper refers to the average value of three months from September to November, and the climate state is the average value of 30 years from 1991 to 2021. The main research method used in this paper is comprehensive analysis. The southern region of China includes multiple stations within the range of

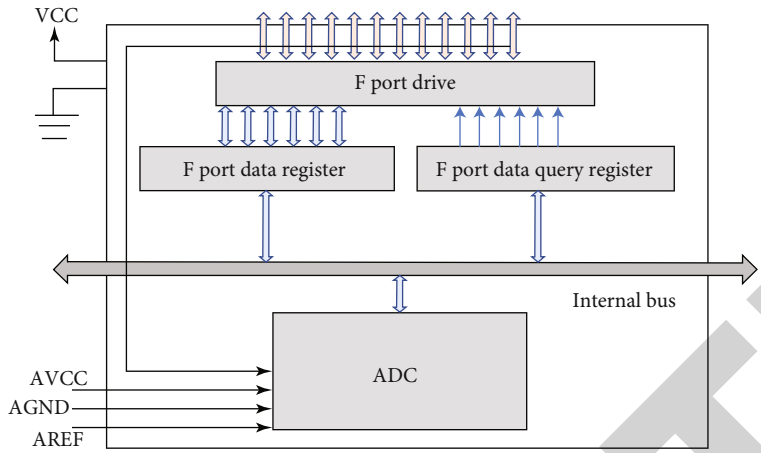

Figure 4: PF port function diagram.

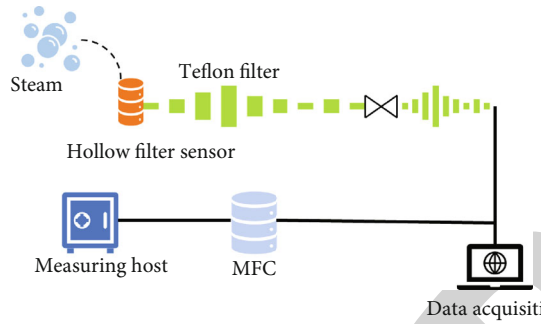

Figure 5: Schematic diagram of water vapor measurement device with hollow fiber sensor.

Figure 6: Distribution map of meteorological stations.

20°~32° N and 98°~122.5° E. The distribution of stations is shown in Figure 6.

4.2. Data Processing. According to the principle of obtaining water vapor by intelligent sensors, the station pressure is a necessary meteorological parameter for Saastamoinen model to calculate the zenith static delay. It is the most effective method to obtain the station air pressure through the meteorological sensor provided by the intelligent sensor. However, generally speaking, most intelligent sensor stations are mainly used for geodetic research and are not equipped with corresponding meteorological sensors, which limits the acquisition of high spatial-temporal resolution water vapor information. Era interim product provided by European mesoscale weather prediction center can obtain layered meteorological data, which makes it possible to obtain station pressure by interpolation.

The spatial resolution of era interim product used in this paper is $0.5^\circ \times 0.5^\circ$-layered meteorological data; each layer includes potential, temperature, relative humidity, and other related data. Using the interpolation method proposed by Villafuerte and Matsumoto [20], find the nearest two pressure layers j and $j+1$ according to the height z of the station to be interpolated, and then, select the four grid points around according to the location of the station. After determining the four grid points of the two pressure layers j and $j+1$ closest to the location of the station, carry out vertical interpolation, and then, carry out horizontal interpolation to the four grid points vertically interpolated to the height z of the station, and finally, obtain the pressure of the station. The specific process is shown in Figure 7 below.

In the process of vertical interpolation, four adjacent grid nodes need to be selected according to the location of the stations to be interpolated. Assuming that the node number is k and the four grid points are k_1, k_2, k_3, and k_4, respectively, extract the air pressure and potential height of the two isobaric surfaces closest to the height Z of the station, and then, calculate the elevation between the two floors. The formula is as follows:

$$H_p^k = \frac{h_{j+1}^k - h_j^k}{\ln P_j^k - \ln P_{j+1}^k}, \tag{7}$$

where H_p^k is the elevation; h_{j+1}^k and h_j^k are the potential heights of the upper and lower layers of k grid points, respectively; and P_{j+1}^k and P_j^k are the air pressure values of the upper and lower layers of k grid points. Therefore, the

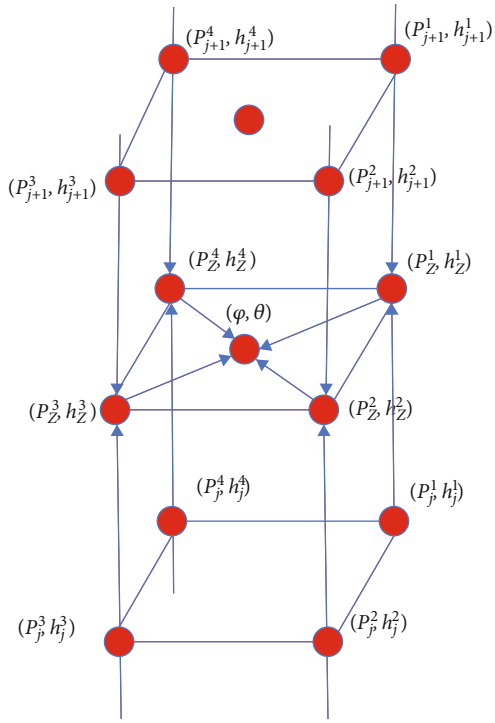

Figure 7: Schematic diagram of ERA-interim product interpolation air pressure data.

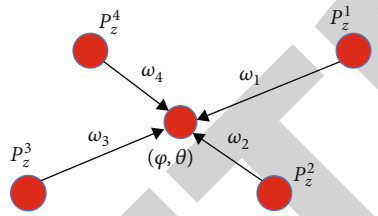

Figure 8: Inverse distance weighted interpolation principle.

pressure value P^k_z of the four grid points at the height z of the station can be expressed as

$$P^k_z = P^k \exp\left(-\frac{z - h^k}{H^k_p}\right), \quad (8)$$

where H^k_p is the elevation, h^k is the potential height of the two pressure layers closest to the height of the station, and P^k is the pressure value corresponding to the potential height of the nearest pressure layer.

Combined with the above two formulas, the air pressure values of the four grid points vertically to the height of the station can be calculated, and then, the air pressure values of the four grid points of the height of the station can be interpolated horizontally. In particular, when the height of the station is lower than the height of the grid point, the bottom two layers of data need to be extrapolated in the vertical interpolation.

In the process of horizontal interpolation, the meteorological data of stations are generally obtained by inverse distance weighting or bilinear interpolation. In this paper, the inverse distance weighting method is selected to determine the weight proportion according to the angular distance between the station position and the grid point. The interpolation principle is shown in Figure 8, and the expression is as follows:

$$\cos\psi^k = \sin\varphi^k \cdot \sin\varphi + \cos\varphi^k \cdot \cos\varphi \cdot \cos\left(\theta^k - \theta\right), \quad (9)$$

where φ^k and θ^k are, respectively, the latitude and longitude of the four grid points around the height of the station; φ and θ are, respectively, the latitude and longitude of the station; and ψ^k is the angular distance between the four grid points and the station.

The weight calculation formula can be expressed as$w^k = (R\psi^k)^{-C}/(R\psi^1)^{-C} + (R\psi^2)^{-C} + (R\psi^3)^{-C} + (R\psi^4)^{-C}$, (10)where R is the average radius of the earth, with a value of 6378.17 km; C is 1; and w^k is the weighting coefficient of grid k horizontal interpolation.

Combined with all the above formulas, the final interpolation expression of pressure interpolation is

$$P_s = w^1 \cdot P^1_z + w^2 \cdot P^2_z + w^3 \cdot P^3_z + w^4 \cdot P^4_z. \quad (10)$$

4.3. ENSO Index. In order to better analyze the characteristic changes of water vapor, the influence of ENSO events on it is studied. In this paper, the Southern Oscillation Index (SOI) and the oceanic Nino index (oni) of the nino3.4 region in the equatorial Pacific provided by the National Oceanic and Atmospheric Administration are selected as ENSO indexes. Because ENSO is the result of the interaction between atmosphere and ocean, El Niño and La Niña are the two extreme stages of ENSO cycle. For the atmosphere, ENSO uses the Southern Oscillation Index for quantitative monitoring. If the SOI is negative, it indicates that the pressure difference between the East and West Pacific Ocean has become smaller, and the index continues to show a negative value; it indicates that El Niño phenomenon occurred in that year; on the contrary, La Niña phenomenon occurred. For the ocean, ENSO uses the marine Niño index to monitor quantitatively. The marine Niño index is calculated from the average sea surface temperature anomaly in the closed area of nino3.4 in the central and eastern tropical Pacific [98]. If the oni lasts for more than five months and exceeds +0.5°C, an El Niño event will occur. If the temperature is lower than -0.5° C for more than five months, La Nina event will occur.

4.4. Relationship between Water Vapor and Monthly Mean SST. Because the ocean ENSO usually uses SST to analyze changes, the temporal resolution provided by ECMWF is 6 h and the spatial resolution is 0.5° × 0.5° seawater surface temperature grid data. Then, the seawater surface temperature data of 12 stations (Figure 9) in the eastern coastal area of China are obtained through bilinear interpolation to study the relationship between water vapor and monthly

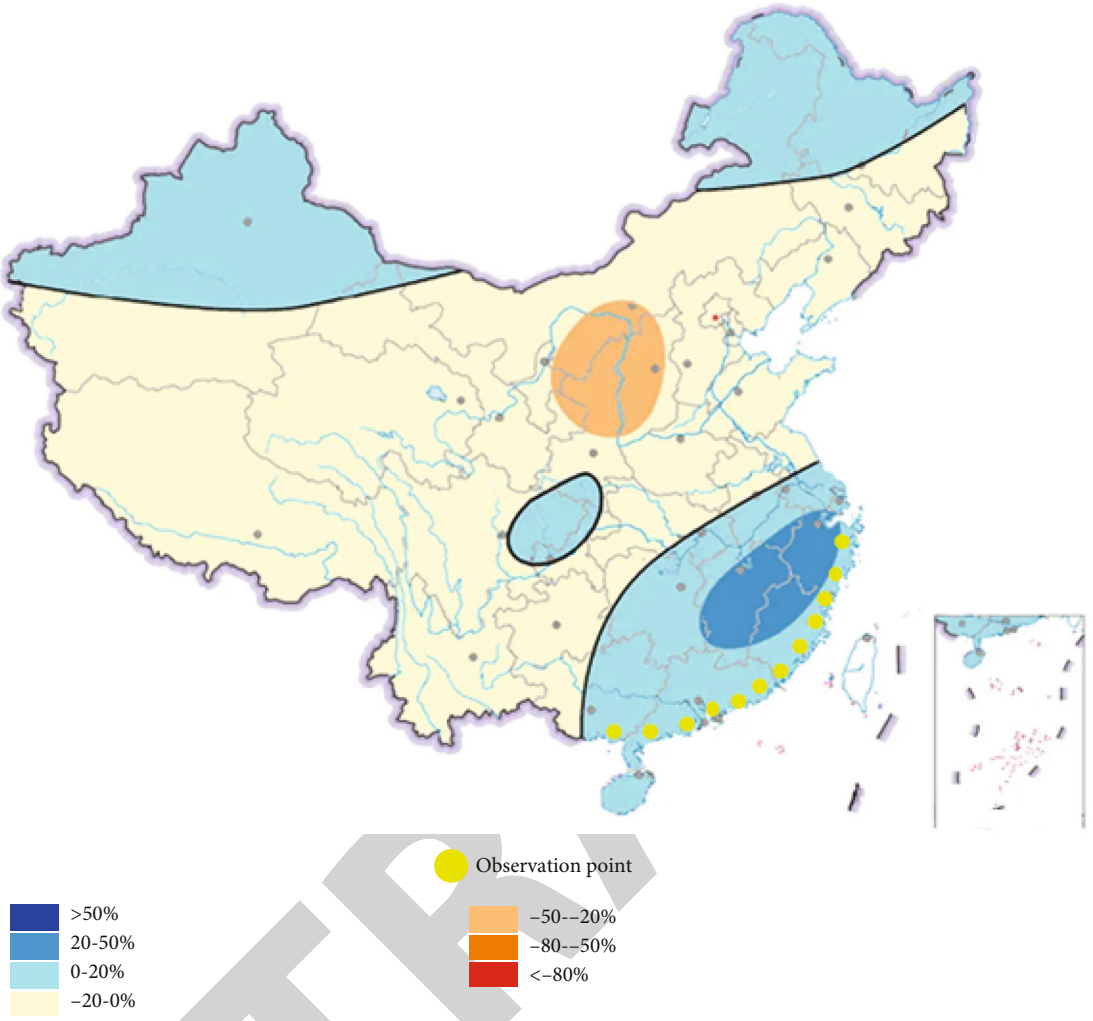

Figure 9: Schematic diagram of 12 meteorological observation points.

average SST in the coastal area of China. Figure 10 shows the scatter diagram of monthly average PWV and SST of four stations in China's coastal areas from 2018 to 2021, and red represents the fitting curve.

It can be seen from Figure 10 that there is a very obvious positive correlation between PWV and SST, and there is a certain relationship between their fluctuations. Therefore, we have made more detailed observations on all stations. Figure 11 shows the correlation coefficients of PWV and SST at 12 stations more comprehensively; PWV increased value is caused by 1 K increase in SST (medium). The relative increase rate of PWV is caused by the increase of 1 K in SST (lower). Figure 11 can reflect the following contents: the correlation coefficient of 10 stations is greater than 0.6, that of 7 stations is greater than 0.8, that of 6 stations is higher than 0.85, and that of 4 stations is 0.9. At the same time, the average correlation coefficient of the stations in the measured area is about 82.13%, and the correlation is very high. According to Figure 11, an increase of 1 K in SST will lead to an increase of 4.17 mm in PWV in some regions of China, an increase of 1 K in SST will lead to an increase of 2.98 mm in PWV within the range of 22.46° N~25.09° N and an increase of 1.82 mm in regions north of 25.09° N. At the same time, according to Figure 11, an increase of 1 K in SST will lead to an increase of 9.74% in PWV of 12 intelligent sensor stations in China's coastal areas. It can be seen that ENSO event has a significant impact on PWV. El Niño phenomenon and La Nina phenomenon will have a serious impact on flood and drought events caused by the increase or decrease of precipitation. However, different ENSO events have different impacts on climate. Therefore, in addition to SST, it is necessary to use water vapor to study ENSO events on a local scale. According to the correlation between water vapor and monthly average SST at 12 intelligent sensor stations in the coastal area of China, it can be found that ENSO events can significantly affect the water vapor in the atmosphere, and at the same time, water vapor can be used to track the evolution of ENSO.

To sum up, the relationship between monthly average PWV and seawater surface temperature is studied by using the water vapor information calculated by 12 coastal intelligent sensor stations. It is found that the correlation coefficient of stations located in the coastal area of China is

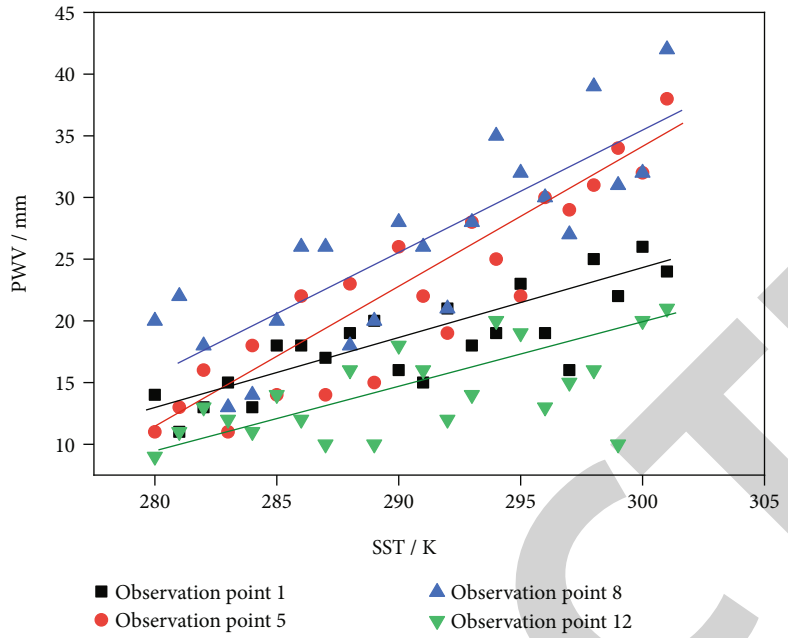

Figure 10: Scatter diagram of water vapor and monthly mean SST at four representative stations.

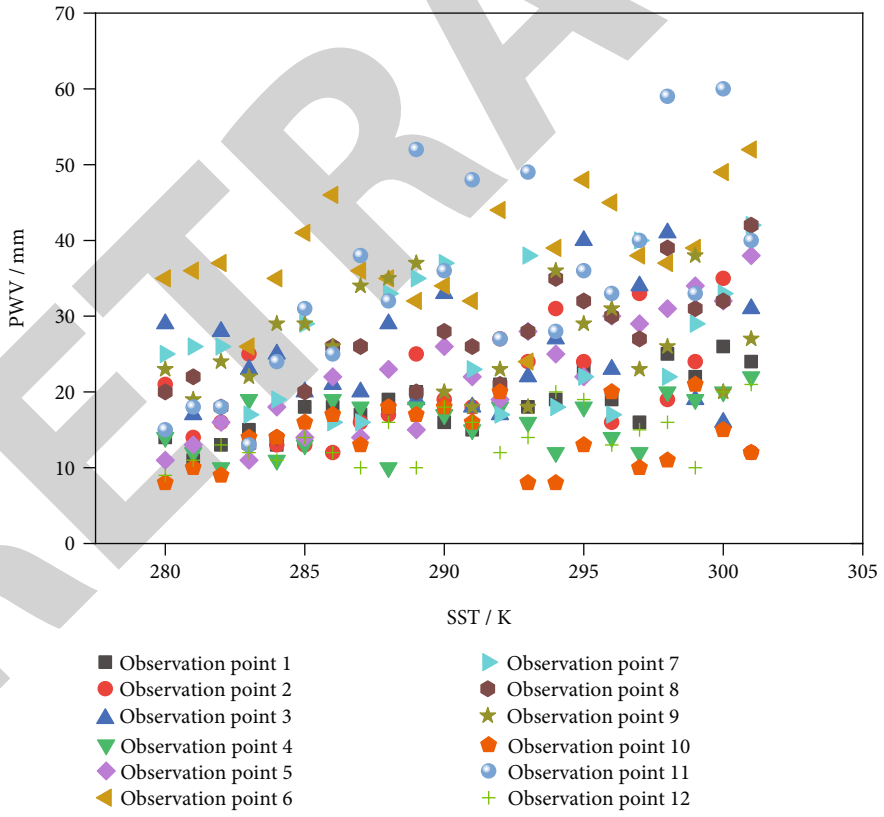

Figure 11: Scatter diagram of water vapor and monthly mean SST at 12 stations.

about 82.13%. An increase of 1 K in SST will lead to an increase of 4.17 mm in PWV in some regions of China, and an increase of 1 K in SST will lead to an increase of 2.98 mm in PWV within the range of 22.46° N~25.09° N in Guangdong Province of China. An increase of 1 K in SST will lead to an increase of 9.74% in PWV at 12 intelligent sensor stations in China's coastal areas. It can be seen that ENSO events have a significant impact on PWV, which also

proves that El Niño has a significant correlation with rainfall changes in China; that is, El Niño has a great correlation with regional water vapor.

5. Conclusion

In recent ten years, with the development of intelligent sensor technology and Walktrap algorithm and the increase of intelligent sensor stations, the advantage of intelligent sensor stations to obtain water vapor is more obvious. Compared with other water vapor detection technologies, intelligent sensor stations can obtain water vapor information with high precision and high spatial-temporal resolution, which will provide an important guarantee for studying the spatial-temporal distribution of water vapor and the changes of various climate models (El Niño). Therefore, this paper further studies this and draws the following conclusions:

Through analysis, it is found that most traditional sensor stations are mainly used for geodetic research and are not equipped with corresponding meteorological sensors, which seriously hinders the acquisition of water vapor information with high spatial-temporal resolution.

This paper does not solve the above information acquisition problem, improves the traditional measuring station, and introduces only sensor technology to obtain information. Through the actual information to obtain feedback, this sensor has superior information acquisition ability.

Based on sensor only technology and Walktrap algorithm, the correlation analysis between El Niño phenomenon and regional water vapor in China is carried out. Through the analysis of the results of 12 meteorological stations in the coastal area of Guangdong Province, it is found that the correlation coefficient of stations located in the coastal area of China is about 82.13%. An increase of 1 K in SST will lead to an increase of 4.17 mm in PWV in some regions of China, and an increase of 1 K in SST will lead to an increase of 2.98 mm in PWV within the range of 22.46° N~25.09° N in Guangdong Province of China. An increase of 1 K in SST will lead to an increase of 9.74% in PWV at 12 GNSS stations in China's coastal areas.

To sum up, it can be found that ENSO events have a significant impact on PWV, which also proves that El Niño has a significant correlation with rainfall changes in China.

Data Availability

The dataset used in this paper is available from the corresponding author upon request.

Conflicts of Interest

The authors declared that they have no conflicts of interest regarding this work.

Acknowledgments

This work was supported by the National Key Research and Development Program of China (2019YFC1510003).

References

[1] K. E. Trenberth, J. Fasullo, and L. Smith, "Trends and variability in column-integrated atmospheric water vapor," *Climate Dynamics*, vol. 24, no. 7-8, pp. 741–758, 2005.

[2] D. H. Staelin, K. F. Kunzi, R. L. Pettyjohn, R. K. L. Poon, R. W. Wilcox, and J. W. Waters, "Remote sensing of atmospheric water vapor and liquid water with the Nimbus 5 microwave spectrometer," *Journal of Applied Meteorology*, vol. 15, no. 11, pp. 1204–1214, 1976.

[3] G. Yamamoto, "Direct absorption of solar radiation by atmospheric water vapor, carbon dioxide and molecular oxygen," *Journal of Atmospheric Sciences*, vol. 19, no. 2, pp. 182–188, 1962.

[4] J. Goldsmith, F. H. Blair, and S. E. Bisson, "Implementation of a turn-key Raman lidar for profiling atmospheric water vapor and aerosols at the US Southern Great Plains climate study site," *office of scientific & technical information technical reports*, 1997.

[5] M. Vesperini, F. M. Breon, and D. Tanre, "Atmospheric water vapor content from spaceborne POLDER measurements," *Geoscience & Remote Sensing IEEE Transactions on*, vol. 37, no. 3, pp. 1613–1619, 1999.

[6] R. Sussmann, T. Borsdorff, M. Rettinger et al., "Technical note: harmonized retrieval of column-integrated atmospheric water vapor from the FTIR network – first examples for long-term records and station trends," *Atmospheric Chemistry and Physics*, vol. 9, no. 22, pp. 8987–8999, 2009.

[7] V. Carrere and J. E. Conel, "Recovery of atmospheric water vapor total column abundance from imaging spectrometer data around 940 nm – sensitivity analysis and application to airborne visible/infrared imaging spectrometer (AVIRIS) data," *Remote Sensing of Environment*, vol. 44, no. 2–3, pp. 179–204, 1993.

[8] C. K. C. Henken, H. Diedrich, R. Preusker, and J. Fischer, "MERIS full-resolution total column water vapor: observing horizontal convective rolls," *Geophysical Research Letters*, vol. 42, no. 22, pp. 10,074–10,081, 2015.

[9] V. Carrère and J. E. Conel, "Comparison of two techniques for recovery of atmospheric water vapor total column abundance from imaging spectrometer data - sensitivity analysis and application to airborne visible/infrared spectrometer (AVIRIS) data," *Aviris The Workshop*, 1990.

[10] X. Zhou, T. Gao, E. S. Takle et al., "Air temperature equation derived from sonic temperature and water vapor mixing ratio for turbulent airflow sampled through closed-path eddy-covariance flux systems," *Atmospheric Measurement Techniques*, vol. 15, no. 1, pp. 95–115, 2022.

[11] G. Gerd, D. Galina, R. Christoph, M. Tomassini, Y. Liu, and M. Ramatschi, "Near real time GPS water vapor monitoring for numerical weather prediction in Germany," *Journal of the Meteorological Society of Japan. Ser. II*, vol. 82, no. 1B, pp. 361–370, 2004.

[12] N. Hajime, K. Ko, and M. Nobutaka, "Data assimilation of GPS precipitable water vapor into the JMA mesoscale numerical weather prediction model and its impact on rainfall forecasts," *Journal of the Meteorological Society of Japan*, vol. 82, no. 1B, pp. 441–452, 2004.

[13] M. Troller, A. Geiger, E. Brockmann, J. M. Bettems, B. Bürki, and H. G. Kahle, "Tomographic determination of the spatial distribution of water vapor using GPS observations," *Advances in Space Research*, vol. 37, no. 12, pp. 2211–2217, 2006.

[14] J. M. Wallace, E. M. Rasmusson, T. P. Mitchell, V. E. Kousky, E. S. Sarachik, and H. von Storch, "On the structure and evolution of ENSO-related climate variability in the tropical Pacific: lessons from TOGA," *Journal of Geophysical Research*, vol. 103, no. C7, pp. 14241–14259, 1998.

[15] H. Weng, K. Ashok, S. K. Behera, S. A. Rao, and T. Yamagata, "Impacts of recent El Niño Modoki on dry/wet conditions in the Pacific rim during boreal summer," *Climate Dynamics*, vol. 29, no. 2-3, pp. 113–129, 2007.

[16] H. Y. Kao and J. Y. Yu, "Contrasting eastern-Pacific and central-Pacific types of ENSO," *American Meteorological Society*, vol. 22, no. 3, pp. 615–632, 2009.

[17] R. C. Izaurralde, R. Sahajpal, X. Zhang et al., "National geodatabase for biofuel simulations and regional analysis of biorefinery siting based on cellulosic feedstock grown on marginal lands," *office of scientific & technical information technical reports*, 2012.

[18] N. K. Larkin, "Global seasonal temperature and precipitation anomalies during El Niño autumn and winter," *Geophysical Research Letters*, vol. 32, no. 16, p. L16705, 2005.

[19] H. Weng, S. K. Behera, and T. Yamagata, "Anomalous winter climate conditions in the Pacific rim during recent El Niño Modoki and El Niño events," *Climate Dynamics*, vol. 32, no. 5, pp. 663–674, 2009.

[20] Q. Marcelino and J. Matsumoto, "The seasonal role of ENSO and monsoon on the interannual variations of rainfall extremes in the Philippine," *Geographical Reports of Tokyo Metropolitan University*, vol. 49, pp. 23–32, 2014.

[21] C. Dong, X. Cui, S. Liu, Z. Jiang, and Y. Wu, "Investigation on the choked mass-flow characteristics of the helium fluid during the Joule-Thomson process in micro-orifice under different high pressures," *Cryogenics*, vol. 122, p. 103416, 2022.

[22] J. R. Pardo, E. Serabyn, and J. Cernicharo, "Submillimeter atmospheric transmission measurements on Mauna Kea during extremely dry El Niño conditions: implications for broadband opacity contributions," *Journal of Quantitative Spectroscopy and Radiative Transfer*, vol. 68, no. 4, pp. 419–433, 2001.

[23] W. Zhang, F. F. Jin, and A. Turner, "Increasing autumn drought over southern China associated with ENSO regime shift," *Geophysical Research Letters*, vol. 41, no. 11, pp. 4020–4026, 2014.

[24] N. Shi, "Forecasting of the large-scale autumn rainfall in China associated with the southern oscillation/El Nio," *Journal of Nanjing Institute of Meteorology*, 1990.

[25] L. U. Xiao-Feng, Z. M. Kuang, L. I. Li, and Y. Liu, "Change characteristics of sugarcane autumn drought in Guangxi, China under background of climate change," *Journal of southern Agriculture*, vol. 47, pp. 217–222, 2016.

[26] J. Wang, S. Wang, Q. Zhang, Y. Li, J. Wang, and J. Zhang, "Characteristics of drought disaster-causing factor anomalies in southwestern and southern China against the background of global warming," *Polish Journal of Environmental Studies*, vol. 24, pp. 2241–2251, 2015.

[27] Y. Qiao, W. Huang, and M. Jian, "Impacts of El Niño-Southern Oscillation and local sea surface temperature on moisture source in Asian-Australian monsoon region in boreal summer," *Aquatic Ecosystem Health & Management*, vol. 15, no. 1, pp. 31–38, 2012.

[28] T. Li, Y. C. Tung, and J. W. Hwu, "Remote and local SST forcing in shaping Asian-Australian monsoon anomalies," *Journal of the Meteorological Society of Japan*, vol. 83, no. 2, pp. 153–167, 2005.

[29] P. Pons and M. Latapy, "Computing communities in large networks using random walks," in *International Conference on Computer & Information Sciences*Springer, Berlin, Heidelberg.

[30] J. H. Ward Jr., "Hierarchical grouping to optimize an objective function," *Journal of the American statistical association*, vol. 58, no. 301, pp. 236–244, 1963.

[31] P. Glynne-Jones, M. J. Tudor, S. P. Beeby, and N. M. White, "An electromagnetic, vibration-powered generator for intelligent sensor systems," *Sensors & Actuators A Physical*, vol. 110, no. 1–3, pp. 344–349, 2004.

[32] Y. Jin, Y. Wen, L. Ping, and X. Dai, "A magnetoelectric, broadband vibration-powered generator for intelligent sensor systems," *Sensors & Actuators A Physical*, vol. 168, no. 2, pp. 358–364, 2011.

[33] Y. C. Cheng and T. G. Robertazzi, "Distributed computation with communication delay (distributed intelligent sensor networks)," *Aerospace & Electronic Systems IEEE Transactions on*, vol. 24, no. 6, pp. 700–712, 1988.

[34] C. A. Worrell, I. P. Giles, and N. A. Adatia, "Erratum: Remote gas sensing with mid-infra-red hollow waveguide," *Electronics Letters*, vol. 28, no. 7, pp. 615–617, 1992.

[35] S. Sato, M. Saito, and M. Miyagi, "Infrared hollow waveguides for capillary flow cells," *Applied Spectroscopy*, vol. 47, no. 10, pp. 1665–1669, 1993.